Available online at www.sciencedirect.com

ScienceDirect

Proceedings of the Combustion Institute 39 (2023) 3249–3258

Proceedings of the Combustion Institute

www.elsevier.com/locate/proci

Flame characterisation of gas-assisted pulverised coal combustion using FPV-LES

Tien Duc Luu [a], Ali Shamooni [a], Oliver T. Stein [a,*], Andreas Kronenburg [a], Sebastian Popp [b], Hendrik Nicolai [b], Henrik Schneider [c], Xu Wen [b], Christian Hasse [b]

[a] *Institut für Technische Verbrennung, Universität Stuttgart, Pfaffenwaldring 31, Stuttgart 70569, Germany*
[b] *Simulation reaktiver Thermo-Fluid Systeme, TU Darmstadt, Otto-Berndt-Straße 2, Darmstadt 64287, Germany*
[c] *Reaktive Strömungen und Messtechnik, TU Darmstadt,Otto-Berndt-Straße 3, Darmstadt 64287, Germany*

Received 4 January 2022; accepted 10 July 2022
Available online 6 September 2022

Abstract

A multiphase flamelet/progress variable (FPV) model for the large eddy simulation (LES) of gas-assisted pulverised coal combustion (PCC) is developed. The target of the simulation is the Darmstadt turbulent gas-assisted swirling solid fuel combustion chamber. The coal particles are treated as Lagrangian point particles, the position, momentum and energy of which are tracked. The gas phase is described by the low-Mach Navier-Stokes equations alongside the Eulerian transport equations of the governing variables for the FPV model. The set of chemical states of the PCC flame is pre-tabulated in a six-dimensional flamelet table and determined by the mixing of the primary fuel stream, volatiles and char off-gases with the oxidising air, the progress of chemical reactions, the interphase heat transfer, as well as sub-grid scale variations. A presumed β-PDF approach for the total mixture fraction is applied to capture sub-grid scale effects. The discrete ordinate method (DOM) with the weighted sum of grey gases model (WSGGM) is employed to model radiation. The FPV-LES results are validated against the experimental evidence and a good agreement of the predicted mean and RMS velocities, as well as the mean gas temperature between experiments and simulations is obtained. The contributions of the pilot, volatile and char off-gas fuel streams to the coal flame are analysed. It is found that most regions of the furnace are dominated by either pilot or volatile combustion, while char conversion only occurs in the far downstream and outer furnace regions. The pilot gas dominates the near-wall region inside the quarl, whereas the volatile gas mainly released from small particles dominates a first volatile combustion zone in the interior of the internal recirculation zone. Larger particles heat up more slowly and release their volatile content further downstream, leading to a secondary volatile combustion zone.

Keywords: LES; FPV; Pulverised coal combustion; Volatile flame; Gas assisted pilot

* Corresponding author.
E-mail addresses: o.stein1@gmx.net, o.stein@itv.uni-stuttgart.de (O.T. Stein).
https://doi.org/10.1016/j.proci.2022.07.080

1. Introduction

Pulverised coal combustion (PCC) is still a major source of primary energy and among the most widespread technologies for generating electrical baseload power. Therefore, the emission of pollutants and greenhouse gases from PCC continues to drive major research efforts to gain deeper insight in its underlying chemical and physical processes with the aim of mitigating pollution and climate change. The four major thermo-physical stages of PCC are heat-up and drying of the particles in a hot environment by convection and radiation, devolatilisation of the light gases initially embedded inside the particles, homogeneous gas combustion and heterogeneous char conversion. These processes primarily occur in consecutive order, but overlaps may exist and require appropriate modelling.

Direct numerical simulation (DNS) studies have been conducted for fully-resolved single particles [1,2] and small particle clusters [2,3]. Two recent examples extended the studies to large particle clouds by means of carrier-phase DNS [4,5]. Nevertheless, the DNS of industrially-relevant applications remains unfeasible at present, due to the large-scale geometries, the wide range of turbulent scales, the enormous number of solid fuel particles, complex interphase coupling processes and the costly homogeneous and heterogeneous chemistry in PCC. A reasonable trade-off between computational cost and accuracy is the large eddy simulation (LES) approach for the gas phase coupled with Lagrangian tracking of the fuel particles, which has been applied in several recent studies on laboratory-scale and semi-industrial coal burners [6–9]. An established combustion modelling approach with limited cost is the tabulated flamelet model that has been widely employed for single phase combustion in the past. An improvement of the flamelet model is provided by the flamelet/progress variable (FPV) approach [10], which is advantageous for capturing the flame dynamics. Watanabe et al. [11] devised FPV for solid fuel combustion with the introduction of two mixture fractions for the mixing of the volatiles and char off-gases with air, with later applications by Rieth et al. [12] and Wen et al. [13] to solid fuel flames in a turbulent mixing layer. The applicability of FPV-LES to laboratory and semi-industrial scale PCC burners has been demonstrated e.g. by Watanabe et al. [14] and Rieth et al. [6]. For gas-assisted PCC, as considered in the present study, Wen et al. [15] reported that a third mixture fraction is needed to characterise the gaseous pilot fuel. Knappstein et al. [7] and Nicolai et al. [9] avoided the third mixture fraction by assuming the volatile composition to correspond to the one of the pilot fuel. However, to consider a more typical volatile composition, a third mixture fraction is inevitable. Wen et al. [16] demonstrated first reasonable FPV-LES results for gas-assisted coal combustion using three mixture fractions.

The gas-assisted coal flame considered in the present study is the turbulent swirl flame experimentally studied at TU Darmstadt. Previous numerical predictions of this combustion chamber were reported in [7,9,16] and based on the earlier operating conditions of Becker et al. [17]. Recently, updated operating conditions and new measurements have been reported by Schneider et al. [18], Meißner et al. [19] and Emmert et al. [20], providing an extensive experimental database for the simulations in this work. The objectives of the present study are

- To accurately model the combustion in swirling gas-assisted coal flames
- To validate the predictions against state-of-the-art measurements
- To characterise the contributions of the pilot, volatile and char off-gas streams to the flame

and our progress towards these aims is discussed in the following sections.

2. Modelling approach

2.1. Gas phase

The gas phase is described by the filtered transport equations of total mass, momentum and the FPV control variables. The control variables are the reaction progress variable Y_C, total enthalpy H (sens. + chem.) and three mixture fractions Z_α, where α denotes the fuel streams originating from the coal volatiles ($\alpha = \text{vol}$) and char off-gases ($\alpha = \text{cog}$). Moreover, in the context of gas-assisted coal flames, a third mixture fraction ($\alpha = \text{pil}$) is required to describe the mixing of the pilot fuel with air. The sub-grid viscosity is closed by the Smagorinsky approach [21]. The assumption $Le = 1$ is invoked and the turbulent mass/heat diffusivities are obtained from turbulent Schmidt/Prandtl numbers set to 0.7 [9]. The reaction progress variable is defined as $Y_C = Y_{CO} + Y_{CO_2} + Y_{H_2O} + Y_{H_2}$ [22–24]. The progress variable source term is retrieved from the flamelet look-up table. Thermal radiation is considered as a source term in the enthalpy transport equation. Radiative heat transfer is modelled by the discrete ordinate method (DOM) using 80 directions, where the absorption/emission coefficients are calculated with the weighted-sum-of-grey-gases model (WSGGM) and the coefficients from [25]. Isotropic scattering by the particles is considered to be dominant, while gas phase scattering is neglected. The gas phase is coupled to the Lagrangian particles via interphase transfer terms [4].

2.2. Solid phase

The solid particles are described within the Lagrangian framework. Their interaction with the gas phase is characterised by the transfer of mass from devolatilisation and char conversion, momentum from drag, gravity and sub-grid dispersion, and energy through convective and radiative heat transfer, as well as the heats of devolatilisation and char conversion. The solid phase governing equations read

$$\frac{dm_p}{dt} = -\left(\dot{m}_{p,\mathrm{devol}} + \dot{m}_{p,\mathrm{char}}\right) \tag{1}$$

$$\frac{d\mathbf{u}_p}{dt} = \frac{\widetilde{\mathbf{u}} - \mathbf{u}_p}{\tau_p} + \left(1.0 - \frac{\bar{\rho}}{\rho_p}\right)\mathbf{g} + \frac{d\mathbf{u}_{p,\mathrm{sgs}}}{dt} \tag{2}$$

$$\frac{dT_p}{dt} = \frac{6\mathrm{Nu}\cdot c_p\bar{\mu}}{\mathrm{Pr}\cdot c_{p,p}\rho_p d_p^2}(T - T_p) + \frac{\varepsilon_p A_p \sigma}{m_p c_{p,p}}\left(\Theta_r^4 - T_p^4\right) + \frac{\dot{Q}_{\mathrm{devol}}}{m_p c_{p,p}} + \frac{\dot{Q}_{\mathrm{char}}}{m_p c_{p,p}}, \tag{3}$$

where ρ_p, d_p, $c_{p,p}$, A_p are the density, diameter, heat capacity, and projected area of the particle, with otherwise standard nomenclature. The particle response time is calculated as $\tau_p = \frac{\rho_p d_p^2}{18\bar{\mu}}(1 + 0.15\,\mathrm{Re}_p^{2/3})^{-1}$. The particle Reynolds number is calculated as $\mathrm{Re}_p = \bar{\rho}|\widetilde{\mathbf{u}} - \mathbf{u}_p|\frac{d_p}{\bar{\mu}}$ and the Nusselt number as $\mathrm{Nu} = 2 + 0.552\,\mathrm{Re}_p^{1/2}\mathrm{Pr}^{1/3}$. The term $\frac{d\mathbf{u}_{p,\mathrm{sgs}}}{dt}$ refers to sub-grid particle dispersion according to the model by Bini and Jones [26]. The particle emissivity ε_p linearly reduces from 0.9 to 0.5 during char burnout [4]. The Eulerian radiation temperature Θ_r is retrieved from the DOM [27,28]. Devolatilisation is described by a competing two-step model with coefficients fitted to the Rhenish lignite coal [18] from the experiments. Darmstadt's Pyrolysis Kinetics Preprocessor (PKP) is employed for fitting, with a multi-step heterogeneous mechanism of PoliMi [29] for a range of heating rates extracted from the simulations of Nicolai et al. [9]. It is assumed that char entirely consists of carbon such that the char off-gases are solely composed of CO and N_2. During devolatilisation, the particle diameter is assumed to remain constant and the density of the particle reduces, whereas constant density and shrinking particle diameter are assumed during char conversion. To consider the effect of devolatilisation in the momentum and energy equations of the particle, a blowing correction is applied. The particle heat capacity, two-step devolatilisation model, char conversion and blowing correction model are similar to [4].

2.3. Combustion modelling

The chemistry tables are generated with the flamelet solver *pyFLUT* coupled with *Cantera* [30] to solve the 1D governing equations of continuity, radial momentum, energy, and species for counterflow diffusion flames. Similar to Wen et al. [15] we employ a three mixture fraction system based on the total mixture fraction Z

$$Z = Z_{\mathrm{pil}} + Z_{\mathrm{vol}} + Z_{\mathrm{cog}} \tag{4}$$

and two mixing ratios [31]

$$A = \frac{Z_{\mathrm{cog}}}{Z_{\mathrm{vol}} + Z_{\mathrm{cog}} + \epsilon},\ B = \frac{Z_{\mathrm{vol}} + Z_{\mathrm{cog}}}{Z_{\mathrm{vol}} + Z_{\mathrm{cog}} + Z_{\mathrm{pil}} + \epsilon} \tag{5}$$

where ϵ represents a small positive number. To consider heat exchange between the gas and solid phase, flamelet tables with various enthalpy levels are generated, accounting for the minimum and maximum enthalpy of the fuel and oxidiser. A normalisation method is employed to the total enthalpy and reaction progress variable to simplify flamelet tabulation [32], leading to normalised quantities H_{norm} and C_{norm} ranging from zero to one. Turbulence-chemistry interactions are considered via integration of a β-PDF for the filtered total mixture fraction $\widetilde{Z}$ and its subgrid variance $\widetilde{Z''^2}$, with the latter obtained algebraically [33]. Homogeneous chemistry is described by the CRECK52 mechanism consisting of 52 species and 452 reactions [2]. The flamelet table is parameterised via $\Phi = \Im(A, B, \widetilde{Z}, \widetilde{Z''^2}, \widetilde{H}_{\mathrm{norm}}, \widetilde{C}_{\mathrm{norm}})$ with dimensions $6 \times 6 \times 101 \times 11 \times 11 \times 101$, resulting in a total size of 25 GB. For efficient parallel computing, a memory abstraction layer (MAL) [34] is employed.

A selected section of the flamelet table is visualised in Fig. 1. The input parameters have been selected to refer to the (pure) pilot and volatile fuel streams as an example. The stoichiometric mixture fractions of the fuels in air are shown as $Z_{\mathrm{pil,st}} = 0.055$ and $Z_{\mathrm{vol,st}} = 0.167$. For the selected values of $C_{\mathrm{norm}} = 1$ and $Z_{\mathrm{var}} = 0$ Fig. 1 shows pure pilot

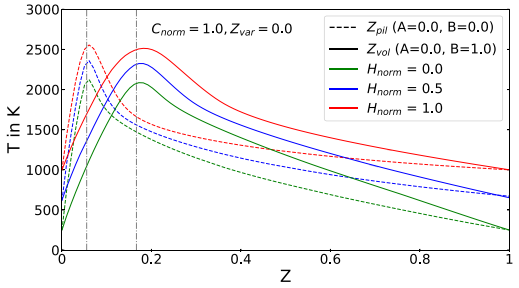

Fig. 1. Selected data from the six-dimensional flamelet table with temperature vs. Z for various enthalpy levels. The input parameters have been selected to refer to either pure pilot or volatile fuel. The vertical dashed-dotted lines indicate the corresponding stoichiometric mixture fractions. (For interpretation of the references to colour in this figure legend, the reader is referred to the web version of this article.)

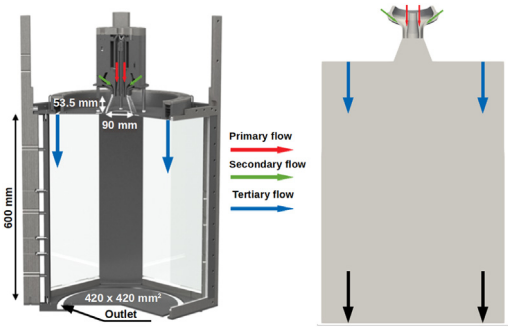

Fig. 2. Geometry and inlet/outlet streams of the TUD burner. Left: Experiment [18], right: Computational domain. (For interpretation of the references to colour in this figure legend, the reader is referred to the web version of this article.)

Table 1
Volume flows and particle load of the investigated operating condition. Primary (I), secondary (II) and tertiary inlet flow (III). Units [m^3/h] for gas and [kg/h] for particles.

I Methane	2.01	II Straight Oxid.	0
I Particles	3.36	II Inclined Oxid.	11.09
I Oxidiser	12.1	III Oxidiser	24.02

and volatile fuel combustion for three levels of normalised enthalpy H_{norm}, with the latter controlling the flamelet boundary temperature.

3. Experimental and numerical setup

The experimental configuration is the swirling gas-assisted solid fuel combustion chamber of TU Darmstadt [7,16,17]. The experimental geometry and computational domain are shown in Fig. 2. The combustion chamber has a cross-section of 420×420 mm^2 and a height of 600 mm. Various fuels and oxidisers may enter the chamber via three inlet streams, namely the primary (I), secondary (II) and tertiary flow (III), where a split into straight and inclined inlet channels allows for a variation of swirl in the secondary flow. Here, we consider coal combustion with air using the injection rates given in Tab. 1, which follows the experiments [18–20]. Coal particles are injected in a rich mixture of methane and air, which serves as a pilot stream to ignite the particles. The secondary flow provides swirling air as oxidiser, while additional air is injected via the tertiary flow to support complete combustion. The contribution of coal and methane to the total thermal input is 50% each, with the stability limit lying at 40–45% methane. Products leave the chamber through an annular orifice at the bottom of the chamber. The surrounding walls of the burner quarl and combustion chamber consist of quartz glass for optical access. Small solid coal particles are used as tracers to determine the gas velocity by PIV [18]. The gas temperature is measured by vibrational O_2-CARS and tomographic absorption spectroscopy (TAS) [20].

The computational mesh is generated with *snappyHexMesh* and contains a total of 3,843,172 hexahedral and split-hexahedral cells, ranging from $\Delta_{x_i} \approx 1$ mm (within the quarl) to 4 mm (downstream). Two thin layers of cells increase the near-wall resolution. A uniform velocity profile is assumed for the inlet patches, matching the experimental mass flow rates from Tab. 1. The inlet boundary conditions for the flamelet control variables are $Z_{\text{pil}} = 0.08456$, $Z_{\text{vol}} = Z_{\text{cog}} = Y_C = 0.0$ and $H = -376,008$ J/kg ($T = 314$ K) for the primary stream. The (cold) pilot mixture is ignited by temporarily adding an artificial source term for the reaction progress variable in the quarl region, which is removed after 250 ms. At the remaining inlet patches all Z_α and Y_{C} are zero, and the enthalpy is set to reflect air at 314 K. An a priori calculation of the two-phase flow and heat transfer upstream of the inlet patches of the simulation domain has been conducted to determine the inlet gas temperature $T_g = 314$ K and particle conditions for the computational domain. A no-slip wall boundary condition is employed at the lateral boundaries and wall temperatures correspond to the experiments [19]. The radiative emissivity of the quartz walls is set to $\varepsilon_w = 0.7$. Rhenish lignite is considered, with its proximate and ultimate analysis given in [18]. After Q-factor adjustment the initial coal composition becomes $Y_{\text{ash}} = 0.0552$, $Y_{\text{VM}} = 0.553$ and $Y_{\text{FC}} = 0.3918$. The volatile composition corresponds to the one of Wen et al. [16], apart from removing H_2S and NH_3 from the volatiles and adding their mass to the ash. The volatile composition is $Y_{\text{CH}_4} = 0.086$, $Y_{\text{C}_2\text{H}_4} = 0.039$, $Y_{\text{C}_6\text{H}_6} = 0.152$, $Y_{\text{CO}} = 0.252$, $Y_{\text{CO}_2} = 0.282$, $Y_{\text{H}_2} = 0.01$ and $Y_{\text{H}_2\text{O}} = 0.179$. The size distribution of the injected coal particles follows ref[7].

The simulations are performed with a low-Mach reactive multiphase solver based on OpenFOAM-v2006. Second-order central differencing is used for spatial discretisation, while a total variation diminishing (TVD) limiter (denoted as *limitedLinear* in OpenFOAM) is employed for convection. Limiters were adopted to obtain bounded scalars and for enhanced simulation stability. Time integration is performed with a backward differencing scheme. A variable time-step of $\Delta t \approx 5\text{e}^{-6}$s is chosen, corresponding to CFL ≈ 0.3. The simulations are first run for single-phase reacting conditions, i.e. without coal particles. Subsequently particles are injected and temporal statistics are started when the particle ensemble in the upstream furnace reaches a steady state (after 2 s). Computations are run for a total physical time of 3.5 s, resulting in 265K statistical samples. A typical FPV-LES run requires ≈150,000 CPUh using 512 AMD-7742 cores on HLRS *Hawk*.

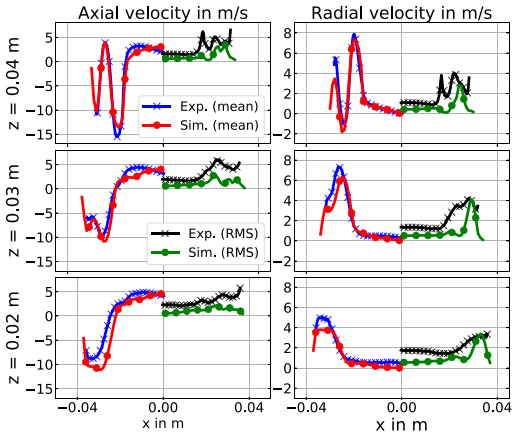

Fig. 3. Comparison of the mean (left-half) and RMS (right-half) axial and radial gas velocity profiles between experiment and simulation inside the quarl.

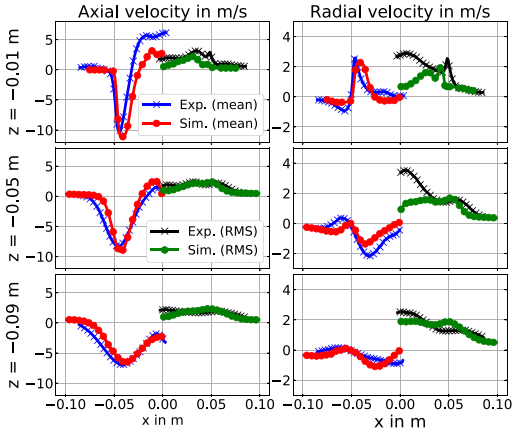

Fig. 4. Comparison of the mean (left-half) and RMS (right-half) axial and radial gas velocity profiles between experiment and simulation downstream of the quarl.

4. Results and discussion

4.1. Numerical validation

A first validation of the simulation results can be obtained by comparing the predicted mean and RMS gas velocities to the experimental data in Figs. 3 and 4. At $z = 0.04$ m in Fig. 3, i.e. just downstream of the primary and secondary inlets to the burner quarl, the two inlet streams can clearly be identified by the negative peaks of axial velocity (which is defined negatively in the positive downstream direction [17]). Conversely, the positive axial velocities observed in the centre of the domain and between the two inlets indicate the inner re-

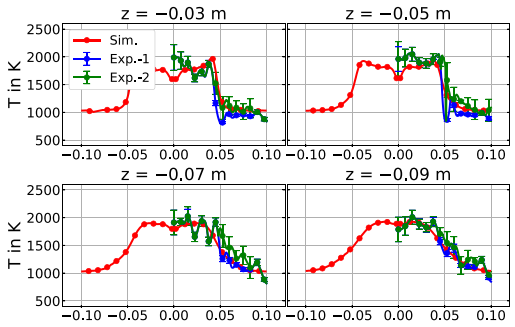

Fig. 5. Comparison of the mean gas phase temperature profiles between experiment and simulation at selected downstream positions. Regular TAS (Exp-1, blue) and TAS overlaid with fluctuation model (Exp-2, green) [20]. (For interpretation of the references to colour in this figure legend, the reader is referred to the web version of this article.)

circulation zone, as well as a small annular recirculation zone that leads to the formation of the side flame (discussed later in Fig. 6 (a)). At $z = 0.04$ m the agreement of the mean velocity predictions and experiments is good, with a slight under-prediction of the velocity peaks in the simulation. The quality of agreement between the simulations and the experiments remains good when moving to the downstream measurement locations $z = 0.03 \ldots -0.09$ m, with somewhat narrower profiles of the predicted mean velocity at intermediate positions $z = 0.02$ and -0.01 m, and a better correspondence again further downstream. Similarly, the predictions of the mean radial velocity profiles are very good throughout, with mild under-predictions of the peak values at $z = 0.03 \ldots 0.02$ m. The comparison of the RMS profiles of the axial and radial gas velocities shows that the level of turbulent fluctuations is generally captured well by the simulations, with minor discrepancies for larger values of $|x|$. The predicted RMS is somewhat lower than the measured one, which is partially attributed to the fact that only the resolved part of the velocity RMS from the LES is compared to the measurements. Larger discrepancies can be observed for the RMS of the radial gas velocity at $z = -0.01$ and -0.05 m for $|x| < 0.05$ m. In these regions volatile gases are released from small particles and a strong momentum exchange with large particles occurs, see Fig. 6 (b) later, which dampens the turbulent fluctuations in the gas phase. The discrepancy may be explained by the fact that the comparison shows predicted gas phase velocities vs. measured velocities obtained from using the coal particles as flow tracers and by minor asymmetries in the PIV measurements. However, given the complexity of the considered multiphase reacting flow, the overall agreement shown in Figs. 3 and 4 is good.

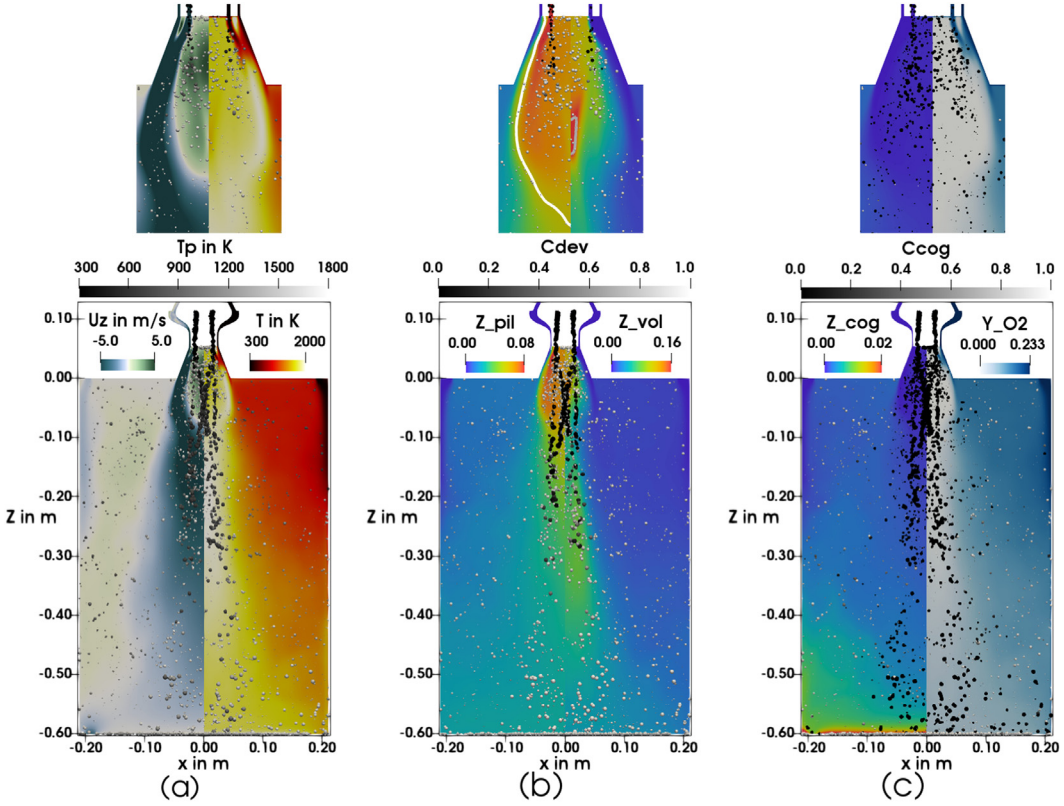

Fig. 6. Time-averaged contours in the central $x - z$ plane of the combustion chamber with a zoom into the quarl region (with only small particles for clarity) in the top row. (a) axial velocity and temperature of the gas, (b) pilot and volatile mixture fraction with isolines $Z_{\mathrm{pil,st}}$ (white) and $Z_{\mathrm{vol,st}}$ (grey), (c) char off-gas mixture fraction and mass fraction of O_2. An instantaneous snapshot of the coal particles is overlaid, where particles are scaled by diameter and coloured according to (a) temperature T_p, (b) devolatilisation progress C_{dev} and (c) char conversion progress C_{cog}. (For interpretation of the references to colour in this figure legend, the reader is referred to the web version of this article.)

This finding is confirmed by the comparison of the mean gas temperatures from simulations and experiments along the radial coordinate shown at different downstream positions in Fig. 5. The overall agreement between the FPV-LES predictions and the experimental evidence is good, with the predicted temperature mostly lying well inside the experimental scatter. The only exception is the under-prediction of the gas temperature near the centreline at $z = -0.03$ and -0.05 m. A fuel composition of $\approx 80\%$ volatiles and $\approx 20\%$ pilot fuel can be found at these axial locations on the centreline. As the peak temperature of the pilot flame is slightly higher than the one of the volatile flame, see Fig. 1, we attribute the under-prediction of the mean temperature to a slight underestimation of the mixing between pilot and volatiles. As the pilot fuel becomes more dominant at larger radii, the temperature increases and matches the experiment very well, Fig. 5. However, considering the uncertainties of both the simulation approach and the experiments for this complex multi-physics problem, the joint agreement demonstrated in Figs. 3, 4 and 5 is overall satisfactory and the FPV-LES methodology captures both the flow field and flame position accurately.

4.2. Flame analysis

After validating the modelling approach, a first impression of the coal conversion process inside the combustor can be obtained from Fig. 6 which shows time-averaged contours of the principal flame quantities that characterise the multiphase fuel conversion process. The mean gas phase contours are overlaid by instantaneous snapshots of the Lagrangian particles coloured by their temperature T_p, devolatilisation C_{dev} and char conversion C_{cog} progress in Fig. 6 (a), (b) and (c) respectively. C_{dev} and C_{cog} are defined to be 0/1 at the beginning/end of the devolatilisation/char conversion process. In Fig. 6 (a), it can be observed

that in the quarl region the (unswirled) primary and (swirled) secondary flow streams merge rapidly and form a bell-shaped inner recirculation zone mainly composed of hot combustion products. From its injection location at $z = 0$, $x = \pm 0.195$ m the (unswirled) tertiary flow stream initially stays close to the lateral walls of the combustion chamber, developing a large external recirculation zone (green colours on the left half of Fig. 6 (a)). The right frame of Fig. 6 (a) shows that the highest gas temperatures are located inside the burner quarl and along the centreline of the combustion chamber, with increasingly wider profiles of high temperature with increasing downstream distance. Directly at the entrance of the quarl, between the primary and secondary streams, a side flame is established, as was also discussed in an earlier study of the same combustor [7]. While larger particles ($d_p > 100\,\mu m$) leave the burner quarl towards the downstream region, most of the smaller particles are entrained in the inner recirculation zone where they heat up quickly and proceed with their conversion process. Conversely, the large particles heat up more slowly and are mainly converted in the middle and downstream furnace. A comparison of gas temperature from Fig. 6 (a) with the pilot and volatile mass fractions in Fig. 6 (b) shows that the flame is located in regions of large gradients of Z_{pil} in the upstream and of Z_{vol} in the middle and downstream regions. The pilot flame dominates the inner recirculation zone, the outside of which features stoichiometric regions of Z_{pil} (white line). The small coal particles are heated up by the pilot flame and hot combustion products, releasing their volatiles as indicated by their high values of C_{dev}. However, only a limited mass of volatiles is released in the quarl, as indicated by the small region of $Z_{\mathrm{vol,st}}$ (grey line), due to the large particles mainly escaping the inner recirculation zone without significant levels of devolatilisation progress. The higher thermal inertia of the large particles leads to a slower increase of C_{dev} and, therefore, a later release of volatile matter, indicated by the regions with increased values of Z_{vol} in the main furnace from $z = -0.15$ ... -0.4 m. However, in regions where large particles start their conversion process the mean values of Z_{vol} show that the stoichiometric value is not reached, while instantaneous snapshots of Z_{vol} (not shown for brevity) reveal that locally around individual coal particles, although values of $Z_{\mathrm{vol}} > Z_{\mathrm{vol,st}}$ are reached, only small local volatile flames are stabilised. The left side of Fig. 6 (c) shows the mixture fraction of the char off-gases. No char conversion can be observed in the quarl region and regions near the centreline, as indicated by both Z_{cog} and C_{cog}. This can be explained by the absence of oxygen in these regions, which has been fully consumed by the combustion of the pilot fuel and coal volatiles, see right side of Fig. 6 (c). However, significant levels of char conversion can be observed at the bottom of

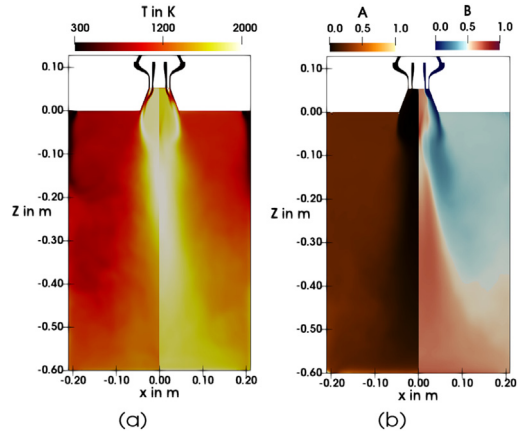

Fig. 7. Time-averaged gas quantities in the central $x - z$ plane. a) Temperature contours of the pilot-only flame (single phase, left half) and piloted coal flame (multiphase, right half), (b) flamelet input parameters A and B (multiphase). (For interpretation of the references to colour in this figure legend, the reader is referred to the web version of this article.)

the combustion chamber. Here, particles are clustered and due to the sufficient amount of oxygen, provided from the tertiary stream, char conversion proceeds.

The flame is now analysed in terms of the contributions of the various fuel streams to combustion. As was observed in Fig. 6 (c) char conversion only occurs in the downstream and outer regions of the furnace, whereas the inner and upstream zones are dominated by the pilot and volatile streams. Therefore, the present paragraph focuses on the characteristics of the pilot and volatile flame. Fig. 7 (a) compares the mean gas temperature from the coal flame (multiphase, right half) to an auxiliary simulation of a pilot-only flame without coal particles (single phase, left half). Lower temperatures can be observed in the internal recirculation zone of the coal flame when compared to the pilot-only flame, which is attributed to the coal particles and volatile gases absorbing heat from the surrounding gas phase. Different visual flame lengths can be seen in Fig. 7 (a), where the pilot-only flame reaches $z = -0.25$ m and the coal flame $z = -0.4$ m. The peak temperature for both flames is similar, which is reasonable due to the tabulated temperatures shown in Fig. 1. A clear differentiation of the contributions of the pilot and volatile fuel to the coal flame can be obtained from the flamelet input parameters A and B, the temporal means of which are shown in Fig. 7 (b). In the absence of char conversion in the upper furnace A and B from Eq. (5) can be used to uniquely identify a pilot-only flame by $A = B = 0$, whereas $A = 0$, $B = 1$ indicates are pure volatile flame. A flame from mixed pilot and volatile fuel is obtained for $A = 0$ and

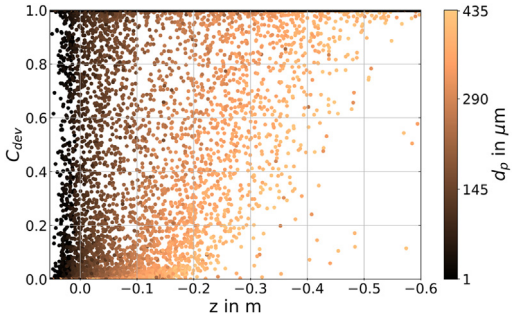

Fig. 8. Scatterplot of particle devolatilisation progress C_{dev} vs. z-coordinate coloured by the particle diameter.

$0 < B < 1$. In Fig. 7 (b), the mixing ratio A attains values of zero in the upstream and central part of the furnace, confirming the presence of pilot and/or volatile fuel and the absence of char conversion in these regions. The mixing ratio B illustrates two major flame zones where A is zero, with the blue regions for B indicating the pilot as the main fuel source, whereas red colours for B refer to volatile fuel. The pilot fuel dominates the outside of the internal swirl-stabilised recirculation zone and the external recirculation zone. The volatile fuel dominates the interior of the internal recirculation zone up to $z = -0.05$ m and a secondary downstream volatile combustion zone spanning from $z = -0.1 \ldots -0.6$ m with increasingly wider profiles with increasing downstream distance. Hence, in the mean, volatile combustion proceeds in a small upstream region inside the quarl where mainly fuel from the smallest particles is consumed, and in a secondary volatile combustion zone in the centre of the downstream furnace, where the volatile fuel from the larger particles is burnt. This is confirmed in Fig. 8 which shows a scatter plot of the particle devolatilisation progress C_{dev} vs. the downstream z-coordinate coloured by the particle diameter. It can be observed that the majority of small particles completes its devolatilisation progress in the upstream recirculation region, whereas most large particles only reach $C_{\text{dev}} = 1$ in the downstream furnace, resulting in the two separated zones of volatile combustion.

5. Conclusions

In the present work a comprehensive model for the turbulent combustion of piloted pulverised solid fuels, namely a six-dimensional multiphase FPV-LES approach, is proposed and validated. The modelling approach is applied to predict a swirl-stabilised piloted coal flame in the TU Darmstadt solid fuel combustion chamber. The simulation results are validated against the experimental evidence and radial profiles of the mean and RMS gas velocities, as well as the mean gas temperature show a good accordance between experiments and simulations. When analysing the contributions of the pilot, volatile and char off-gas fuel streams to the coal flame, it is found that the pilot gas mainly dominates the area near the wall inside the quarl and the external recirculation zone. Two separate zones of volatile combustion are identified. A small upstream region in the interior of the inner recirculation zone that is mainly fuelled by recirculating small particles and a secondary volatile flame region in the centre of the downstream furnace that is dominated by the larger coal particles. Char conversion is negligible where pilot and volatile fuel dominates, but char combustion occurs near the bottom of the combustion chamber and at larger radii.

Declaration of Competing Interest

The authors declare that they have no known competing financial interests or personal relationships that could have appeared to influence the work reported in this paper.

Acknowledgments

The authors acknowledge the financial support by the Deutsche Forschungsgemeinschaft for project numbers 238057103, 450158108 and 215035359. We are grateful for HPC time on HLRS Hawk and bwHPC.

References

[1] S. Farazi, M. Sadr, S. Kang, M. Schiemann, N. Vorobiev, V. Scherer, H. Pitsch, Resolved simulations of single char particle combustion in a laminar flow field, Fuel 201 (2017) 15–28, doi:10.1016/j.fuel.2016.11.011.

[2] G.L. Tufano, O.T. Stein, B. Wang, A. Kronenburg, M. Rieth, A.M. Kempf, Coal particle volatile combustion and flame interaction. Part I: Characterization of transient and group effects, Fuel 229 (2018) 262–269, doi:10.1016/j.fuel.2018.02.105.

[3] T. Sayadi, S. Farazi, S. Kang, H. Pitsch, Transient multiple particle simulations of char particle combustion, Fuel 199 (2017) 289–298, doi:10.1016/j.fuel.2017.02.096.

[4] M. Rieth, A.M. Kempf, A. Kronenburg, O.T. Stein, Carrier-phase DNS of pulverized coal particle ignition and volatile burning in a turbulent mixing layer, Fuel 212 (2018) 364–374, doi:10.1016/j.fuel.2017.09.096.

[5] A. Shamooni, P. Debiagi, B. Wang, T.D. Luu, O.T. Stein, A. Kronenburg, G. Bagheri, A. Stagni, A. Frassoldati, T. Faravelli, A.M. Kempf, X. Wen, C. Hasse, Carrier-phase DNS of detailed NO_x formation in early-stage pulverized coal combustion with fuel-bound nitrogen, Fuel 291 (2021) 119998, doi:10.1016/j.fuel.2020.119998.

[6] M. Rieth, F. Proch, A.G. Clements, M. Rabaçal, A.M. Kempf, Highly resolved flamelet LES of a semi-industrial scale coal furnace, Proc. Combust. Inst. 36 (2017) 3371–3379, doi:10.1016/j.proci.2016.08.089.
[7] R. Knappstein, G. Kuenne, L.G. Becker, F. di Mare, A. Sadiki, A. Dreizler, J. Janicka, Large Eddy Simulation of a novel gas-assisted coal combustion chamber, Flow Turbul. Combust. 101 (2018) 895–926, doi:10.1007/s10494-018-9910-x.
[8] Y. Chen, O.T. Stein, A. Kronenburg, J. Xing, K. Luo, K.H. Luo, C. Hasse, Analysis of gas-assisted pulverized coal combustion in Cambridge Coal Burner CCB1 using FPV-LES, Energy Fuels 34 (2020) 7477–7489, doi:10.1021/acs.energyfuels.0c00317.
[9] H. Nicolai, G. Kuenne, R. Knappstein, H. Schneider, L.G. Becker, C. Hasse, F. di Mare, A. Dreizler, J. Janicka, Large Eddy Simulation of a laboratory-scale gas-assisted pulverized coal combustion chamber under oxy-fuel atmospheres using tabulated chemistry, Fuel 272 (2020) 1–16, doi:10.1016/j.fuel.2020.117683.
[10] C.D. Pierce, P. Moin, Progress-variable approach for large-eddy simulation of non-premixed turbulent combustion, J. Fluid. Mech. 504 (2004) 73–97, doi:10.1017/S0022112004008213.
[11] J. Watanabe, K. Yamamoto, Flamelet model for pulverized coal combustion, Proc. Combust. Inst. 35 (2015) 2315–2322, doi:10.1016/j.proci.2014.07.065.
[12] M. Rieth, A.M. Kempf, O.T. Stein, A. Kronenburg, C. Hasse, M. Vascellari, Evaluation of a flamelet/progress variable approach for pulverized coal combustion in a turbulent mixing layer, Proc. Combust. Inst. 37 (2019) 2927–2934, doi:10.1016/j.proci.2018.05.150.
[13] X. Wen, M. Rieth, A. Scholtissek, O.T. Stein, H. Wang, K. Luo, A.M. Kempf, A. Kronenburg, J. Fan, C. Hasse, A comprehensive study of flamelet tabulation methods for pulverized coal combustion in a turbulent mixing layer - Part I: A priori and budget analyses, Combust. Flame 216 (2020) 439–452, doi:10.1016/j.combustflame.2019.05.046.
[14] J. Watanabe, T. Okazaki, K. Yamamoto K. Kuramashi, A. Baba, Large-eddy simulation of pulverized coal combustion using flamelet model, Proc. Combust. Inst. 36 (2017) 2155–2163, doi:10.1016/j.proci.2016.06.031.
[15] X. Wen, Y. Luo, H. Wang, K. Luo, H. Jin, J. Fan, A three mixture fraction flamelet model for multi-stream laminar pulverized coal combustion, Proc. Combust. Inst. 37 (2019) 2901–2910, doi:10.1016/j.proci.2018.05.147.
[16] X. Wen, H. Nicolai, H. Schneider, L. Cai, J. Janicka, H. Pitsch, C. Hasse, Flamelet LES of a swirl-stabilized multi-stream pulverized coal burner in air and oxy-fuel atmospheres with pollutant formation, Proc. Combust. Inst. 38 (2021) 4141–4149, doi:10.1016/j.proci.2020.05.061.
[17] L.G. Becker, H. Kosaka, B. Böhm, S. Doost, R. Knappstein, M. Habermehl, R. Kneer, J. Janicka, A. Dreizler, Experimental investigation of flame stabilization inside the quarl of an oxyfuel swirl burner, Fuel 201 (2017) 124–135, doi:10.1016/j.fuel.2016.09.002.
[18] H. Schneider, S. Valentiner, N. Vorobiev, B. Böhm, M. Schiemann, V. Scherer, R. Kneer, A. Dreizler, Investigation on flow dynamics and temperatures of solid fuel particles in a gas-assisted oxy-fuel combustion chamber, Fuel 286 (2021) 119424, doi:10.1016/j.fuel.2020.119424.
[19] C. Meißner, H. Schneider, E. Sidiropoulos, J.I. Hölzer, T. Heckmann, B. Böhm, A. Dreizler, T. Seeger, Inves- tigation on wall and gas temperatures inside a swirled oxy-fuel combustion chamber using thermographic phosphors, O_2 rotational and vibrational CARSInvestigation on wall and gas temperatures inside a swirled oxy-fuel combustion chamber using thermographic phosphors, o_2 rotational and vibrational cars, Fuel 289 (2021) 119787, doi:10.1016/j.fuel.2020.119787.
[20] J. Emmert, H. Schneider, C. Meißner, E. Sidiropoulos, J.I. Hölzer, T. Seeger, B. Böhm, A. Dreizler, S. Wanger, Characterization of temperature distributions in a swirled oxy-fuel coal combustor using tomographic absorption spectroscopy with fluctuation modelling, Appl. Energy Combust. Sc. 6 (2021) 100025, doi:10.1016/j.jaecs.2021.100025.
[21] J. Smagorinsky, General circulation experiments with the primitive equations. I. The basic experiment, Mon. Weather Rev. 91 (1963) 99–164, doi:10.1175/1520-0493(1963)091<0099:GCEWTP>2.3.CO;2.
[22] M. Ihme, Y.C. See, LES flamelet modeling of a three-stream MILD combustor: Analysis of flame sensitivity to scalar inflow condition, Proc. Combust. Inst. 33 (2011) 1309–1317, doi:10.1016/j.proci.2010.05.019.
[23] S. Popp, F. Hunger, S. Hartl, D. Messig, B. Coriton, J.H. Frank, F. Fuest, C. Hasse, LES flamelet-progress variable modeling and measurements of a turbulent partially-premixed dimethyl ether jet flame, Combust. Flame 162 (2015) 3016–3029, doi:10.1016/j.combustflame.2015.05.004.
[24] M. Vascellari, G.L. Tufano, O.T. Stein, A. Kronenburg, A.M. Kempf, A. Scholtissek, C. Hasse, A flamelet/progress variable approach for modeling coal particle ignition, Fuel 201 (2017) 29–38, doi:10.1016/j.fuel.2016.09.005.
[25] L.J. Dorigon, G. Duciak, R. Brittes, F. Cassol, M. Galarça, F.H.R. França, WSGG correlations based on HITEMP2010 for computation of thermal radiation in non-isothermal, non-homogeneous H_2O/CO_2 mixtures, Int. J. Heat Mass Transfer 64 (2013) 863–873, doi:10.1016/j.ijheatmasstransfer.2013.05.010.
[26] M. Bini, W.P. Jones, Large-eddy simulation of particle-laden turbulent flows, J. Fluid Mech. 614 (2008) 207–252, doi:10.1017/S0022112008003443.
[27] M. Stöllinger, B. Naud, D. Roekaerts, N. Beishuizen, S. Heinz, PDF modeling and simulations of pulverized coal combustion Part 2: Application, Combust. Flame 160 (2013) 396–410, doi:10.1016/j.combustflame.2012.10.011.
[28] H. Nicolai, X. Wen, F.C. Miranda, D. Zabrodiec, A. Massmeyer, F. di Mare, A. Dreizler, C. Hasse, R. Kneer, J. Janicka, Numerical investigation of swirl-stabilized pulverized coal flames in air and oxy-fuel atmospheres by means of large eddy simulation coupled with tabulated chemistry, Fuel 287 (2021) 119429, doi:10.1016/j.fuel.2020.119429.
[29] S. Sommariva, T. Maffei, G. Migliavacca, T. Faravelli, E. Ranz, A predictive multi-step kinetic model of coal devolatilization, Fuel 89 (2010) 318–328, doi:10.1016/j.fuel.2009.07.023.

[30] D.G. Goodwin, H.K. Moffat, R.L. Speth, Cantera: An object-oriented software toolkit for chemical kinetics, thermodynamics, and transport processes, 2018, (https://www.cantera.org/). Version 2.4.0. doi:10.5281/zenodo.1174508
[31] X. Wen, H. Wang, Y. Luo, K. Luo, J. Fan, Evaluation of flamelet/progress variable model for laminar pulverized coal combustion, Phys. Fluids 29 (2017) 083607, doi:10.1063/1.4999335.
[32] D. Messig, M. Vascellari, C. Hasse, Flame structure analysis and flamelet progress variable modelling of strained coal flames, Combust. Theo. Mod. 21 (2017) 700–721, doi:10.1080/13647830.2017.1290279.
[33] C.D. Pierce, P. Moin, A dynamic model for subgrid-scale variance and dissipation rate of a conserved scalar, Phys. Fluids 10 (1998) 3041–3044, doi:10.1063/1.869832.
[34] S. Weise, D. Messig, B. Meyer, C. Hasse, An abstraction layer for efficient memory management of tabulated chemistry and flamelet solutions, Combust. Theo. Mod. 17 (2013) 411–430, doi:10.1080/13647830.2013.770602.